CrossMark

Equilibrium Eccentricity of Accreting Binaries

Jonathan Zrake[1], Christopher Tiede[2] , Andrew MacFadyen[2] , and Zoltán Haiman[3]
[1] Department of Physics and Astronomy, Clemson University, Clemson, SC 29634, USA; jzrake@clemson.edu
[2] Center for Cosmology and Particle Physics, Physics Department, New York University, New York, NY 10003, USA
[3] Department of Astronomy, Columbia University, New York, NY 10027, USA

Abstract

Using high-resolution hydrodynamics simulations, we show that equal-mass binaries accreting from a circumbinary disk evolve toward an orbital eccentricity of $e \simeq 0.45$, unless they are initialized on a nearly circular orbit with $e \lesssim 0.08$, in which case they further circularize. The implied bi-modal eccentricity distribution resembles that seen in post-AGB stellar binaries. Large accretion spikes around periapse impart a tell-tale, quasiperiodic, bursty signature on the light curves of eccentric binaries. We predict that intermediate-mass and massive black hole binaries at $z \lesssim 10$ entering the LISA band will have measurable eccentricities in the range of $e \simeq 10^{-3} - 10^{-2}$, if they have experienced a gas-driven phase. On the other hand, GW190521 would have entered the LIGO/Virgo band with undetectable eccentricity $\sim 10^{-6}$ if it had been driven into the gravitational-wave regime by a gas disk.

1. Introduction

Gas accretion onto orbiting binaries is of general importance to the understanding of a range of astrophysical systems. Examples include massive black hole binaries (Begelman et al. 1980), binary protostars (e.g., Alves et al. 2019, and references therein), post-AGB stellar binaries (e.g., Mathieu et al. 1991), and stellar-mass objects embedded in accretion disks in galactic nuclei (Baruteau et al. 2011). Each of these binaries may be surrounded by, and accrete from, a circumbinary gas disk at some stage of its life.

The gas flow established from the binary–disk interaction exerts gravitational forces on the binary, and directly transfers mass and momentum to it, leading to evolution of the system's orbital elements over time. Epochs of gas accretion could thus be responsible for the present-day eccentricities of many binary systems. The accretion dynamics might also be reflected in the light curves of all types of accreting binaries, and could be sensitive to the system's orbital parameters. It is therefore valuable to understand how binary eccentricities evolve in response to accretion, and in turn how their accretion signals behave as a function of eccentricity.

It has been suggested as early as 1992 (Artymowicz 1992) that the eccentricities of accreting comparable-mass binary stars might be driven up as high as $e \gtrsim 0.5$–0.7, based on linear theory (Goldreich & Tremaine 1980) and clues from early smooth-particle hydrodynamics (SPH) simulations (Artymowicz et al. 1991; Lubow & Artymowicz 1992). Armitage & Natarajan (2005) and Cuadra et al. (2009) have both reported simulations of binaries evolving to $e \gtrsim 0.3$ (see their Figures 2 and 8 respectively). More recent SPH simulations (Roedig et al. 2011) showed unequal mass binaries with $M_2/M_1 = 1/3$ evolving toward an eccentricity between 0.6 and 0.8. Moving-mesh hydrodynamic simulations (Muñoz et al. 2019) of equal-mass binaries have exhibited eccentricity growth at $e = 0.1$, and suppression at $e = 0.5$ and 0.6.

In this Letter we report simulations showing that circumbinary accretion tends to evolve equal-mass binaries toward a stable eccentricity $e_{eq} \simeq 0.45$, and that this evolution is fast, in

the sense that a system should reside near e_{eq} following the accretion of only $\sim 1\%$ of its mass. Eccentric binaries are found to exhibit rich temporal accretion signals, showing distinct waveforms, pulse structures, and duty cycles in different eccentricity regimes. Here we address a few key applications of these results to binary stars and protostars, and massive black hole binaries. Details of the physical mechanism of gas-driven eccentricity evolution and further applications will be reported in Zrake et al. (2021, in preparation).

Our simulation setup is briefly summarized in Section 2. In Section 3, we report the computed eccentricity evolution as a function of e. We also provide an empirical fitting formula $\dot{e}(e)$ that can be used in modeling of binary populations. In Section 4 we present the accretion signatures of binaries at a range of eccentricities. In Section 5 we discuss gravitational-wave signatures of eccentric binaries, and predict the eccentricity of massive black hole binaries entering the LISA band. We summarize our results in Section 6.

2. Simulation Setup

We simulated the coupled evolution of an eccentric, equal-mass binary with a circumbinary gas disk. The disk is thin, two-dimensional, and locally isothermal with orbital Mach number $(h/r)^{-1} = 10$. Viscous stress is included with an α-viscosity prescription with $\alpha = 0.1$. Accretion onto the binary components is modeled by subtracting mass and momentum in a circular region of radius $r_{sink} = 0.02a$, where a is the binary semimajor axis. We utilize an initial condition in which the disk has a finite extent, and is thus free to expand outwards as it relaxes under the viscous stress. This setup captures binary evolution in the quasi-steady relaxed state of the disk, as well as the slow secular depletion of the surface density (Muñoz et al. 2020). The code is Mara3: a grid-based higher-order Godunov code with static mesh refinement. The simulation setup and hydrodynamic equations of motion are described fully in Tiede et al. (2020).

We ran 64 simulations of eccentric binaries: low- and high-resolution suites of 32 runs each, with eccentricities ranging
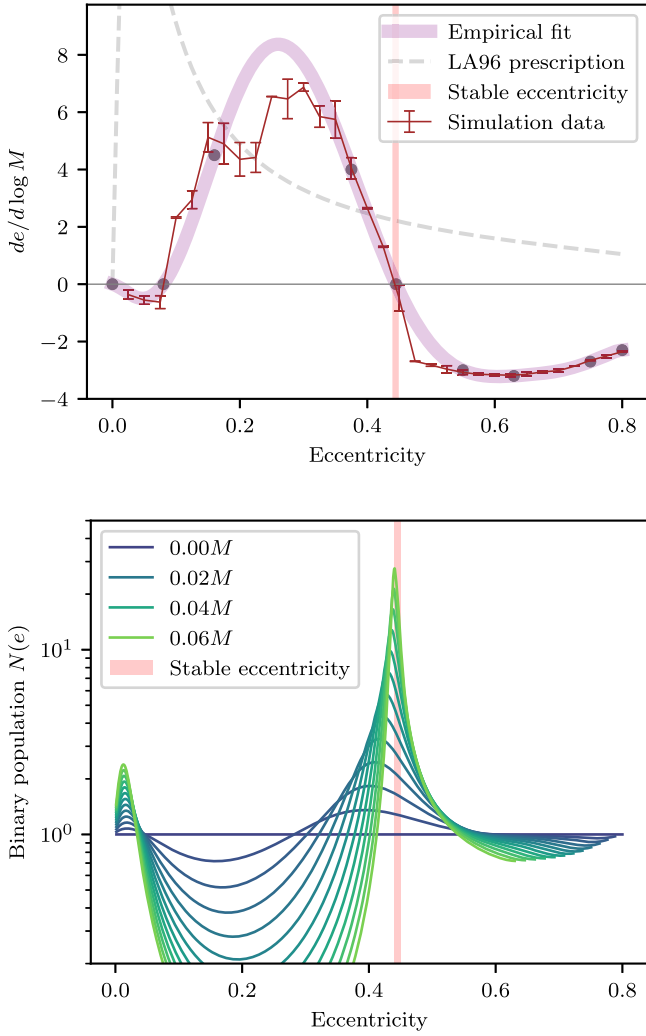
Table 1
Table of Control Points Used in the Empirical Fitting Relation between the Binary Eccentricity e Rate of Eccentricity Driving $de/d \log M$ Shown in Figure 1

j	e_j	$(de/d \log M)_j$	a_j
0	0.000	+0.0	+0.0000e0
1	0.080	+0.0	−5.5122e0
2	0.160	+4.5	−5.5540e2
3	0.375	+4.0	+1.2667e4
4	0.445	+0.0	−7.5392e4
5	0.550	−3.0	+2.0419e5
6	0.630	−3.2	−2.8660e5
7	0.750	−2.7	+2.0393e5
8	0.800	−2.3	−5.8380e4

Note. The first two columns define an eighth degree Lagrange interpolating polynomial, shown in Equation (2), and the final column contains the equivalent coefficients written in the direct polynomial basis, Equation (3).

Figure 1. Top: the rate of eccentricity evolution, per relative accreted mass, as a function of the binary eccentricity. Uncertainties are obtained by comparing two suites of 32 runs each, which are identical except for their numerical resolution. The purple band shows an empirical fit given by Equation (2), and the gray circles show the control points from Table 1. The light dashed curve shows a commonly used prescription for $\dot{e}(e)$ from Lubow & Artymowicz (1996; formally valid up to $e = 0.2$), and the light dashed–dotted curve shows the extrapolation used by Dermine et al. (2013). Bottom: gas-driven evolution of a binary population $N(e)$, after accretion of given fractions (up to 6%) of the binary mass M. The evolution is determined by using the empirical fit shown in the top panel.

from 0.025 to 0.8. The low-resolution runs had grid spacing $\Delta x \simeq 0.016a$, and the high-resolution runs had $\Delta x \simeq 0.012a$. Numerical convergence of the result was established by comparing the two suites, as shown in the error bars in Figure 1. Each run was evolved for three viscous relaxation times $t_{\rm visc}$, corresponding to roughly 2000 orbits. Stationarity was confirmed by inspecting the time series of the total mass accretion rate $\dot{M}$, the torque $\dot{L}$, and work $\dot{E}$ done by the disk on the binary. $\dot{L}$ and $\dot{E}$ include both the gravitational and accretion forces. The rate of change of the binary eccentricity is given by

$$\frac{\dot{e}e}{1-e^2} = \frac{\dot{M}}{M} + \frac{3\dot{\mu}}{2\mu} - \frac{\dot{E}}{2E} - \frac{\dot{L}}{L}, \tag{1}$$

where $\mu \equiv M_1 M_2 / M$ is the reduced mass and M_1 and M_2 are the component masses. The binary mass $M \equiv M_1 + M_2$ is much larger than the mass accreted per disk relaxation time,

consistent with the orbital eccentricity being fixed in each simulation. The gravitational and accretion forces that comprise the time derivatives on the right side of Equation (1), all scale linearly with $\dot{M}$. Thus, measurements of eccentricity evolution, which we report in terms of $\langle \dot{e} \rangle / \langle \dot{M} \rangle \equiv de/dM$, are valid in the limit $t_{\rm visc} \dot{M} \ll M$. Time averages $\langle \cdot \rangle$ were computed from $t = t_{\rm visc}$ to $3 t_{\rm visc}$.

3. Eccentricity Evolution

Figure 1 shows the rate of eccentricity change, per relative accreted mass ($de/d \log M$), as a function of the eccentricity. The four simulations at low eccentricity $e = 0.025$ through $e = 0.075$ exhibit $\dot{e} < 0$, and these binaries would thus be circularized by their interaction with the disk. Somewhere in the range $e = 0.075$–0.1, $\dot{e}$ increases abruptly and becomes positive. Eccentricity driving then increases in strength to a maximum $de/d \log M \simeq 7$ in the run with $e = 0.3$. The rate of eccentricity driving then smoothly declines, becoming negative between $e = 0.425$ and $e = 0.45$. The zero-crossing of $\dot{e}$ represents the stable eccentricity $e_{\rm eq}$, since binaries to the left of $e_{\rm eq}$ evolve to the right, and those to the right of $e_{\rm eq}$ evolve to the left.

The essential characteristics of the function $\dot{e}(e)$ are well captured by the empirical fit, shown in the light purple band in Figure 1,

$$\frac{de}{d \log M} \simeq \sum_{j=0}^{8} \left(\frac{de}{d \log M} \right)_j \prod_{\substack{k=0 \\ j \neq k}}^{8} \frac{e - e_k}{e_j - e_k}, \tag{2}$$

where the control points e_j and $(de/d \log M)_j$ define a Lagrange interpolating polynomial and are given in Table 1. An equivalent formula in terms of polynomial coefficients a_j, also given in Table 1, is

$$\frac{de}{d \log M} \simeq \sum_{j=0}^{8} a_j e^j. \tag{3}$$

To demonstrate the utility of the empirical fit, we use it to evolve the distribution $N(e)$ of a sample population of accreting binaries forward in time. The bottom panel of Figure 1 shows this evolution, starting from a flat initial distribution $N(e) =$ constant over the range $0 < e < 0.8$ and assuming that the accretion rate
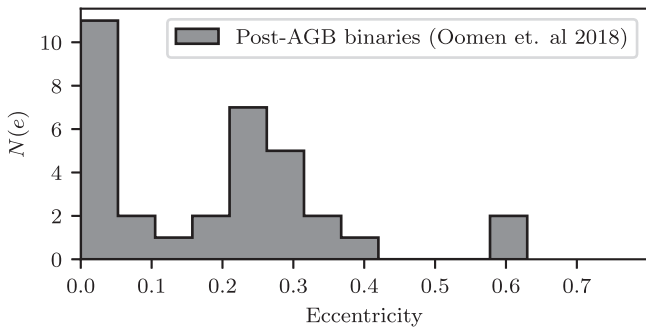
Figure 2. Distribution of the eccentricity measurements of the 32 post-AGB stellar binaries reported in Oomen et al. (2018). Each system has a period of $\lesssim 10$ yr and should thus have been tidally circularized in the AGB phase.

does not depend on e. After accreting a few percent of the binary mass the eccentricity distribution develops a pronounced peak around the equilibrium eccentricity $e_{eq} \simeq 0.45$. A secondary peak of circular binaries also emerges, populated by the binaries starting with $e \lesssim 0.08$. Few binaries remain with intermediate eccentricities in the range of $0.08 \lesssim e \lesssim 0.45$ and binaries initialized with $e \gtrsim 0.45$ are gradually depleted as well.

3.1. Eccentricity of Post-AGB Stellar Binaries

The computed eccentricity evolution $\dot{e}(e)$ may help explain the surprisingly high eccentricity of many post-AGB stellar binaries. These stars have previously ejected their hydrogen envelopes, and should have circularized via mass transfer in dense winds or Roche lobe overflow as they moved off the main sequence, provided their orbital periods are $\lesssim 10$ years (Pols et al. 2003). Post-AGB binaries on close orbits are nevertheless observed to have high eccentricities up to $e \approx 0.45$ (Jorissen et al. 1998; Oomen et al. 2018), as shown in Figure 2.

Tidal interaction with a circumbinary disk has been suggested to account for the eccentricity of the post-AGB binaries (Waters et al. 1998). Several studies, including those of Dermine et al. (2013), Antoniadis (2014), and Oomen et al. (2020), have modeled gas-driven eccentricity evolution using a prescription for $\dot{e}(e)$ suggested in Lubow & Artymowicz (1996). This prescription, which we denote as $\dot{e}_{LA}(e)$, is shown for comparison with our results in Figure 1. Note that since $\dot{e}_{LA}(e) > 0$ for all e including $e \rightarrow 0$, the Lubow & Artymowicz (1996) prescription predicts spontaneous excitation of eccentricity from the well-circularized orbits expected in late-state AGB binaries, and is thus incompatible with the observed abundance of accreting and yet nearly circular binaries. In contrast, our results can account for the bi-modality in $N(e)$, as evidenced by the similarity between the simple predictions in Figure 1 and the observed distribution in Figure 2, but only if binaries are somehow perturbed onto slightly noncircular orbits by some other means. In other words, if the eccentricity distribution shown in Figure 2 is indeed reflective of gas-driven binary evolution, it leaves open the question of how the high-e systems were nudged above the $e \simeq 0.08$ threshold.

4. Accretion Signatures

Figure 3 shows the total accretion rate $\dot{M}$ as a function of time, over 20-orbit time windows, for binaries with increasing eccentricity. The $e = 0.025$ case shown in the top-most panel exhibits features that are now well-established for circular equal-mass binaries (MacFadyen & Milosavljević 2008; Shi et al. 2012; Farris et al. 2014; Muñoz et al. 2019; Duffell et al. 2020): $\dot{M}$ is

modulated relatively smoothly in the orbital phase, with excursions of $\sim 25\%$ above and below the mean accretion rate. The enhancement in $\dot{M}$ every ~ 5 orbits is due to an $m = 1$ density structure (or "lump"), which is itself on an eccentric orbit around the binary at $r \sim 3a$, and transports a surplus of mass onto the binary at each periapse passage.

At $e = 0.1$ the accretion rate develops a distinct sawtooth pattern. Most orbits exhibit two local maxima in $\dot{M}$, the first preceding periapse by roughly one-fifth of an orbit, and the other occurring precisely at periapse. The first of the two peaks is usually of larger amplitude. Note that the sawtooth pattern shows good regularity between orbits, and that the five-orbit accretion enhancement is no longer present at $e = 0.1$. This is due to suppression of the disk eccentricity, which is reported in detail in Zrake et al. (2021, in preparation), and is consistent with Miranda et al. (2017) who observed disappearance of the lump at $e = 0.1$. At $e = 0.25$ the sawtooth pattern changes shape, now resembling a fast-rise exponential-decay type pulse, with the highest peak now always preceding periapse by a fraction of an orbit. The waveform develops modest irregularity, varying in amplitude somewhat from one orbit to the next. This trend continues to $e = 0.4$; the accretion is now strongly concentrated in the pre-periapse spike, and the waveform develops increasing irregularity between orbits. At $e = 0.75$ the waveform is even noisier and more irregular, exhibiting multiple accretion spikes during most orbits. The peak-to-trough ratio of $\dot{M}$ increases from ~ 2 for near-circular orbits to ~ 100 for $e \gtrsim 0.4$.

4.1. Accretion in Binary T-Tauri Stars

Our computed accretion signatures for binaries at a range of eccentricities may shed light on modulated and pulsed accretion observed in T-Tauri stellar binaries. For example, visual inspection of Figure 9 from Jensen et al. (2007) suggests that modulating light curves of UZ Tau ($e \simeq 0.14$–0.33) might be a better fit to the sawtooth pattern we see at $e \simeq 0.25$, than the sinusoidal waveform obtained by Artymowicz & Lubow (1996) from SPH simulations of an $e = 0.1$ binary, which was the best simulation data those authors had available at that time. Martín et al. (2005) reported observations of UZ Tau in which the brightest peaks occurred at orbital phase 0.88, even though several observations were made closer to periastron, an effect which may reflect our computed signatures at $e = 0.25$ and $e = 0.4$ in which the peak accretion rate systematically precedes periastron by 10%–20% of an orbit.

The increasing irregularity of the accretion signal we see in our simulations at $e \gtrsim 0.4$ appears consistent with the incomplete duty cycle of pulsed emission from the high eccentricity system DQ Tau ($e \simeq 0.57$; Muzerolle et al. 2019). Mathieu et al. (1997) reported significant nondetections of accretion pulses in as many as 35% of pariastrons. Irregular light curves of DQ Tau were also reported in Kóspál et al. (2018) and Tofflemire et al. (2017). Bary & Petersen (2014) observed an accretion flare around *apastron*. Importantly, accretion pulses at the half-orbital period do begin to emerge in our simulations, infrequently at $e \simeq 0.55$ and become common toward $e = 0.8$ (see orbits 1217, 1218, and 1224 in the bottom panel of Figure 3). Muñoz & Lai (2016) had speculated that the half-orbit accretion pulses, not evident in their simulations of a binary with $e = 0.5$, might have been numerically unresolved. However, observations of the high-e system DQ Tau, together
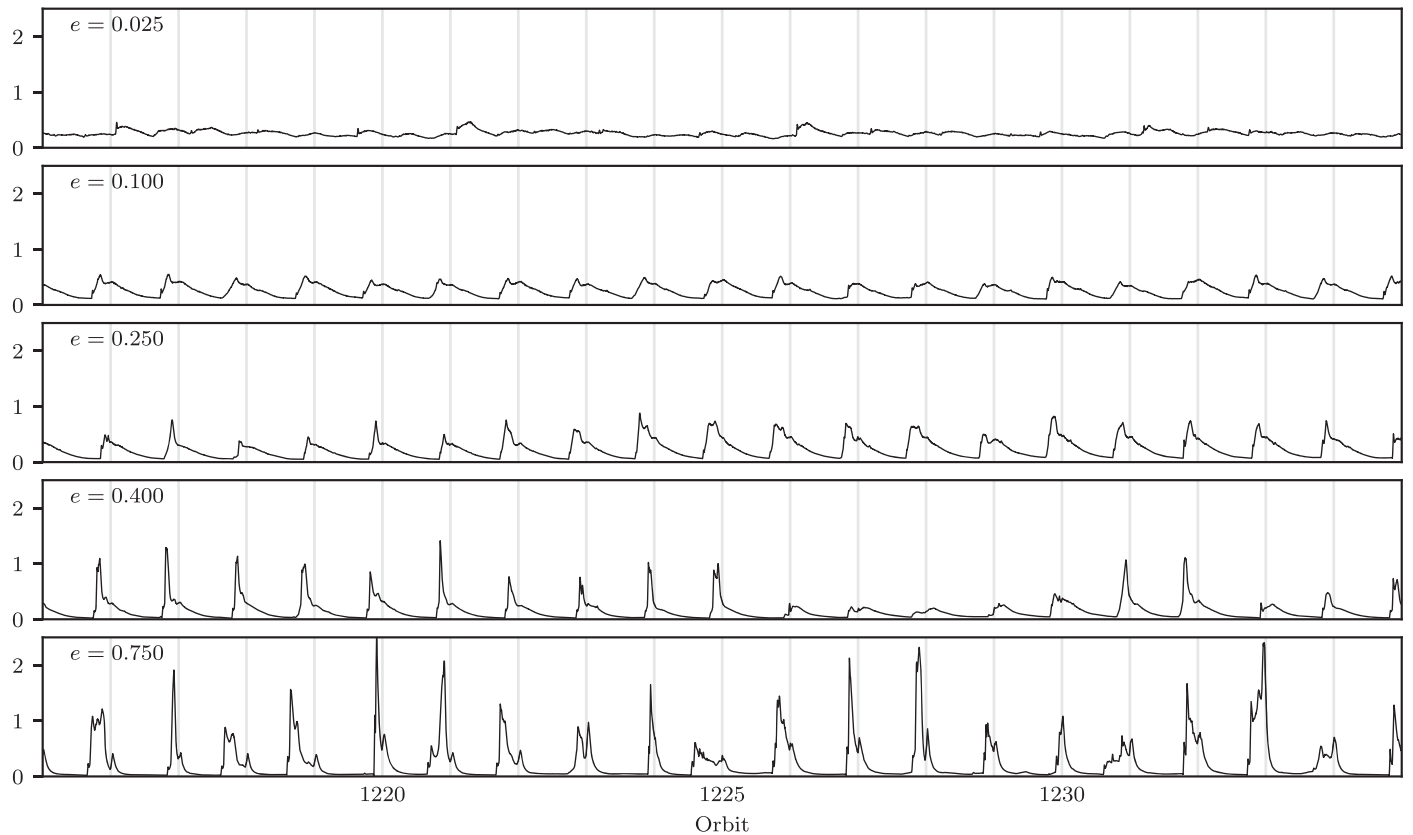
Figure 3. Time series of the total accretion rate $\dot{M}$, in arbitrary units, at representative binary eccentricities: $e = 0.025, 0.1, 0.25, 0.4, 0.75$ from top to bottom. The light vertical lines indicate periapse passages.

with simulations reported here, suggest that half-period spikes emerge only at $e \gtrsim 0.55$.

4.2. Electromagnetic Signatures of MBHBs

Our simulations indicate that MBHBs in the gas-driven regime (nominally at separations $\gtrsim 0.01$ pc for $10^{8-9} M_\odot$ BHs; e.g., Haiman et al. 2009) will have eccentricity $\sim e_{\rm eq}$. Optical variabilities of widely separated binary quasars in the gas-driven regime are thus expected to resemble the sawtooth accretion patterns in the fourth panel of Figure 3, if their emission is dominated by accretion onto the black holes. More compact MBHBs evolving in the gravitational-wave (GW) regime should, on the other hand, exhibit light curves characteristic of circular binaries. Dozens of binary quasar candidates have now been identified in large-scale optical time-domain surveys (e.g., Graham et al. 2015; Charisi et al. 2016; Chen et al. 2020), most of which exhibit sinusoidally modulating light curves. If these systems are indeed MBHBs, they are either well into the GW-driven regime, or are exhibiting variability not directly connected to the accretion, such as Doppler modulations (D'Orazio et al. 2015). We also note that the algorithms used to search for periodicities among the large number of quasar light curves, based on Lomb–Scargle periodograms and their variants, are sensitive primarily to quasisinusoidal variability, and may miss the bursty or sawtooth like periodicities. This should motivate the use of different search algorithms to mitigate a selection bias against eccentric binaries.

An intriguing exception is the periodic quasar candidate J0252 reported recently by Liao et al. (2020). This system exhibits significantly nonsinusoidal variability, which was interpreted in that study as evidence for a binary of unequal masses, by

comparing its light curve to the simulated accretion signatures from Farris et al. (2014) of a binary with $M_2/M_1 = 0.11$. Although the light curves appear rather sawtooth, as if they might also fit a mildly eccentric binary, we find the unequal mass scenario is indeed more likely, since J0252 is separated by $\lesssim 10^{-3}$ pc and almost certainly in the GW-driven regime. A systematic comparison between the computed light curves of eccentric versus unequal mass systems could help us to differentiate otherwise ambiguous binary quasars.

The blazar OJ287, which exhibits a 12 yr optical period, has been postulated to be an eccentric binary black hole. Our results here are not directly applicable to the "standard model" of this source, which involves an unequal mass binary on an orbit tilted with respect to the circumbinary disk, and fits its periodic light curve, with recurring double peaks (see, e.g., Laine et al. 2020 and Dey et al. 2018 and references therein). While our results suggest that an eccentric binary naturally arises even in the coplanar case, the observed regularity of the OJ287 pulses seems incompatible with our computed accretion signals for eccentric binaries.

5. Gravitational-wave Signatures

5.1. LISA

Massive black holes (MBHBs) with $M \approx 10^{2-7} M_\odot$ produce gravitational waves (GWs) that could be detected by the planned space interferometer LISA in the days to years leading up to their coalescence (e.g., Amaro-Seoane et al. 2017). LISA is expected to be sensitive to source eccentricities as small $e \sim 10^{-3}$, and it has been argued (Armitage & Natarajan 2005; Cuadra et al. 2009) that residual eccentricity from a gas-driven

episode might be imprinted on MBHBs in the LISA band. Here we update and expand on those calculations, taking into account our computed equilibrium eccentricity $e_{eq} \simeq 0.45$, updated LISA sensitivity curves from Robson et al. (2019), and a wider range of source masses and redshifts.

Milosavljević & Phinney (2005) proposed that beyond the so-called decoupling radius, at which the viscous timescale in the nearby disk exceeds the GW inspiral time, the binary runs away without the disk being able to follow. However, Farris et al. (2015) and Tang et al. (2018) found that angular momentum transfer by shocks occurs on the orbital timescale, enabling the inner disk to follow the rapidly inspiraling binary. We therefore include the disk torques throughout the inspiral, in contrast with prior works, which assumed that disk torques are abruptly suppressed at the nominal decoupling radius (e.g., Armitage & Natarajan 2005; Roedig et al. 2011).

The notion of a decoupling radius is only valid if binaries are hardened ($\dot{a} < 0$) by gas driving, but this need not always be the case: circular equal-mass binaries surrounded by $h/r = 0.1$ disks absorb angular momentum from the disk and are instead widened (Miranda et al. 2017; Tang et al. 2017; Muñoz et al. 2019; Duffell et al. 2020; Tiede et al. 2020). However, in Zrake et al. (2021, in preparation) we show that binaries at the stable eccentricity experience gas-driven hardening, at a rate of $d \log a / d \log M \sim -1$.

We therefore initialize widely separated binaries in a gas-driven phase at the stable eccentricity e_{eq}, and evolve them as they inspiral due to the combined effects of the gas disk and GW emission. Given Equation (2) for $de/d \log M$, and the assumption that binaries accrete at the Eddington rate, we obtain equations for $\dot{a}_{gas}$ and $\dot{e}_{gas}$. We then add the post-Newtonian terms for $\dot{a}_{GW}$ and $\dot{e}_{GW}$ from Peters (1964) to account for gravitational-wave driving, and solve the resulting differential equation for the combined influence of gas and GWs numerically.

Figure 4 shows the result of this calculation for sample binaries initiated in the gas-dominated phase with $e = 0.45$. The top panel shows the trajectory in characteristic strain h_c versus observed frequency f, for four representative binaries of different chirp masses, and assuming a 4 yr observation time (i.e., LISA mission lifetime). The bottom panel shows the trajectory of the same sample binaries as they evolve through eccentricity and observed frequency. Each system will be detectable by LISA at least 3 yr before it merges, and at that time its eccentricity is 0.003. Thus we predict that 3 yr prior to merger, LISA binaries delivered to the GW regime by gas accretion will have a measurable eccentricity $\gtrsim 10^{-3}$.

Binaries just entering the LISA band will have still higher eccentricity. Figure 5 shows, as a function of the binary chirp mass and redshift, the orbital eccentricity at the time the source is first detectable (i.e., the characteristic strain is above LISA's noise). Note that very nearby sources within $\sim$40Mpc will have $e \sim 0.02$–0.1, depending on chirp mass. Sources at $z = 1$ with chirp masses $\mathcal{M} = 10^2$–$10^4 M_\odot$ are predicted to have $e = 0.005$–0.01. These values are larger by a factor of $\sim$few than those obtained in Armitage & Natarajan (2005), but compatible with the estimates of Cuadra et al. (2009).

5.2. PTAs

Supermassive binary black hole ($10^{7-10} M_\odot$) systems generate a stochastic background of low-frequency GWs, which may be consistent with the signal recently measured in NANOGrav's
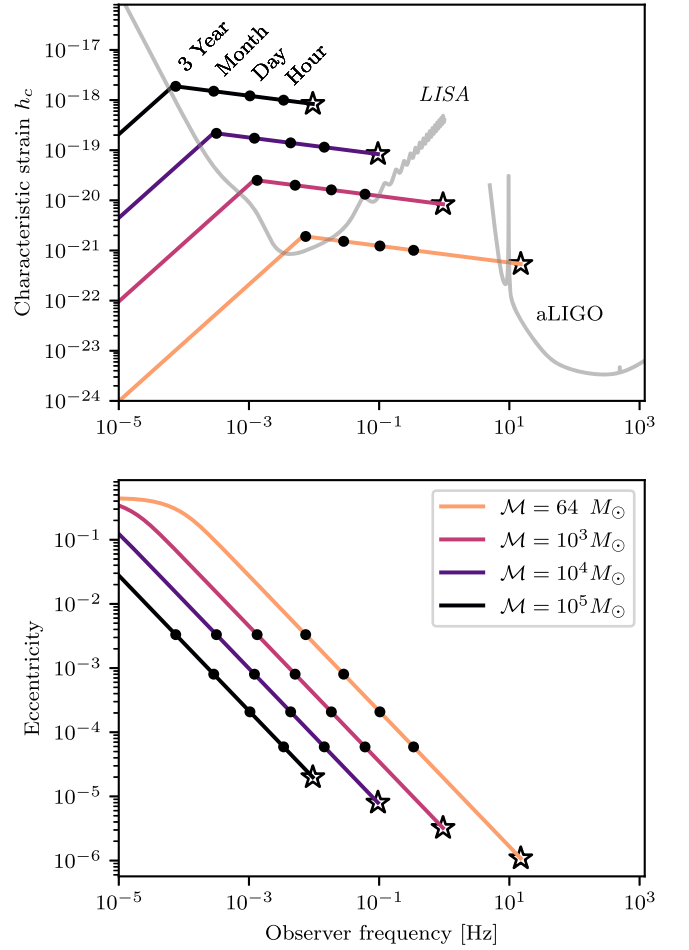

Figure 4. Top: characteristic strain of a sample of four different equal-mass black hole binaries, as they evolve through (observed) frequency f in the gravitational-wave-driven regime (note that $64 M_\odot$ is roughly the chirp mass associated with GW190521). The LISA sensitivity curve $\sqrt{S_n f}$ is shown in gray (Robson et al. 2019). The sources are all located at redshift $z = 1$. The time until merger is indicated in solid black circles, and star symbols mark the innermost stable circular orbit (ISCO). Bottom: eccentricity versus observed frequency for the same sample black hole binaries. The binaries are initialized at $e = 0.45$ near the equilibrium eccentricity obtained in the gas-dominated evolution phase, and circularize due to gravitational radiation as they evolve toward higher frequency.

12.5 yr data (Arzoumanian et al. 2020) and is expected to be confidently detected by further pulsar timing array (PTA) campaigns over the next several years (Mingarelli 2019). Gas disks are known to significantly impact the unresolved stochastic background (Kocsis & Sesana 2011). For example, eccentricity tilts the single-source spectrum (Sesana 2015) by shifting GW power to higher harmonics. Eccentric binaries also harden faster than circular ones, reducing the number of background sources around the decoupling frequency (Sesana 2015). PTAs are also expected to resolve individual sources, and these are likely to be near the fiducial decoupling stage (Kelley et al. 2017). Our results therefore have the potentially significant implication that individual PTA binaries will be highly eccentric, with e at, or not far below, its equilibrium value.

5.3. LIGO/Virgo

Figure 4 shows that if binaries like GW190521, with chirp mass $\sim$64$M_\odot$ and at redshift $z \sim 1$, accrete from circumbinary disks, they will cross through the LISA band with detectable
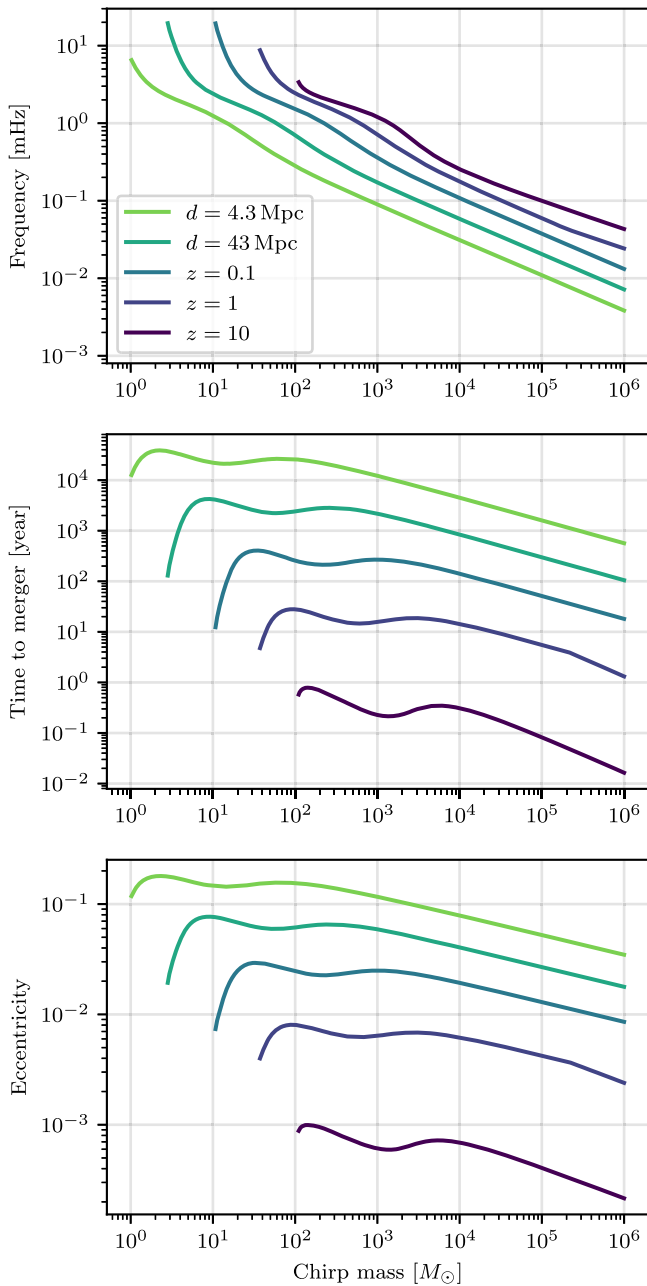
Figure 5. Binary parameters upon entering the LISA band, as a function of the chirp mass $\mathcal{M}$, for sample redshifts from $z = 10$ (dark) down to $z = 10^{-3}$ (light). The frequency (top), merger time (middle), and eccentricity (bottom) are at the time when the binary characteristic strain h_c first intersects the LISA sensitivity curve as shown in Figure 4.

eccentricity $e \sim 5 \times 10^{-3}$. Such events merge in the aLIGO band; however, upon entering it their eccentricity is further suppressed by GW circularization to $e \sim 10^{-6}$. Therefore, the large eccentricities $e \gtrsim 0.1$ and $e \sim 0.7$ suggested in Romero-Shaw et al. (2020) and Gayathri et al. (2020), respectively, cannot be attributed to a circumbinary disk as discussed in this Letter.

6. Summary

We have examined the eccentricity evolution of equal-mass binary systems accreting from a circumbinary gas disk, mapping out the rate of eccentricity change $\dot{e}$ as a function of e in the range

of $e = 0.025$–0.8. Based on a suite of simulations where the disk has aspect ratio $h/r = 0.1$ and viscosity parameter $\alpha = 0.1$, binaries with $e \lesssim 0.08$ are circularized, and those with $e \gtrsim 0.08$ are driven toward an equilibrium eccentricity $e_{eq} \simeq 0.45$. The evolution is fast, in the sense that the binary population develops an order-unity enhancement around e_{eq} after systems have accreted a mere $\sim 1\%$ of their mass.

We provided an empirical fit $\dot{e}(e)$ to our simulation results, for use in population synthesis modeling of accreting black hole and stellar binaries. It predicts an eccentricity distribution $N(e)$ that is bi-modal, and highly suggestive of the population of accreting post-AGB stellar binaries. However, insofar as these systems ought to have been circularized by mass transfer at an earlier stage, they should have remained circular given the modest threshold $e \simeq 0.08$ for eccentricity growth. It suggests either an unknown mechanism to halt circularization in the AGB phase (e.g., Bonačić Marinović et al. 2008), or that the eccentricity of post-AGB stars is not ultimately controlled by accretion from the circumbinary disk (Rafikov 2016).

The temporal signatures of eccentric binary accretion are strikingly diverse. The five-orbit periodicity occurring in circular binaries is suppressed for $e \gtrsim 0.1$. In the range $e \simeq 0.1$–0.4, the periodicity develops a distinct sawtooth shape, and accretion spikes typically precede periapse passage in orbital phase by 10%–20%. At $e \gtrsim 0.4$ the accretion becomes increasingly irregular, and the pulses vary dramatically in amplitude from one orbit to the next. Around $e \gtrsim 0.55$, the accretion pulses begin to spread out in orbital phase, sometimes even occurring around apoapse. We discussed these accretion signals in the context of the spectroscopic proto-stellar binaries UZ Tau and DQ Tau, and found several consistencies with our simulations, including with the orbital phase of the pulses, and their increasing irregularity at high e.

We discussed prospects for the application of eccentric accretion signals for interpreting the light curves of binary quasar candidates. Assuming that the optical variability of these systems reflects BH accretion rate modulations, we predict that the variability is sawtooth in the gas-driven regime ($e \simeq e_{eq}$), and exhibits the well-known five-orbit periodicity only in the GW-driven regime after the orbit has largely circularized.

Finally, we showed that MBHBs that are delivered to the GW regime through binary accretion are likely to enter the LISA band with a measurable eccentricity $10^{-2} - 10^{-3}$. This applies to LISA sources of chirp mass as low as $\sim 10^2 M_\odot$ and as high as $10^4 M_\odot$ out to a redshift $z \sim 10$, or within $z = 1$ and with chirp mass as large as $10^6 M_\odot$. Comparable-mass PTA sources detected around the gas decoupling stage are predicted to be eccentric with $e \simeq 0.4 - 0.5$.

Appendix

Table 1 contains the coefficients used in either of the equivalent empirical fit formulas (Equations (2) or (3)) for $de/d \log M$. A Python function to evaluate Equation (2) is

returned by `scipy.interpolate.BarycentricInterpolator(ej, yj)`, where `ej` and `yj` are the two middle columns of Table 1.

ORCID iDs

Christopher Tiede ● https://orcid.org/0000-0002-3820-2404
Andrew MacFadyen ● https://orcid.org/0000-0002-0106-9013
Zoltán Haiman ● https://orcid.org/0000-0003-3633-5403

References

Alves, F. O., Caselli, P., Girart, J. M., et al. 2019, Sci, 366, 90
Amaro-Seoane, P., Audley, H., Babak, S., et al. 2017, arXiv:1702.00786
Antoniadis, J. 2014, ApJL, 797, L24
Armitage, P. J., & Natarajan, P. 2005, ApJ, 634, 921
Artymowicz, P. 1992, PASP, 104, 769
Artymowicz, P., Clarke, C. J., Lubow, S. H., & Pringle, J. E. 1991, ApJL, 370, L35
Artymowicz, P., & Lubow, S. H. 1996, ApJL, 467, L77
Arzoumanian, Z., Baker, P. T., Blumer, H., et al. 2020, ApJL, submitted (arXiv:2009.04496)
Baruteau, C., Cuadra, J., & Lin, D. N. C. 2011, ApJ, 726, 28
Bary, J. S., & Petersen, M. S. 2014, ApJ, 792, 64
Begelman, M. C., Blandford, R. D., & Rees, M. J. 1980, Natur, 287, 307
Bonačić Marinović, A. A., Glebbeek, E., & Pols, O. R. 2008, A&A, 480, 797
Charisi, M., Bartos, I., Haiman, Z., et al. 2016, MNRAS, 463, 2145
Chen, Y.-C., Liu, X., Liao, W.-T., et al. 2020, MNRAS, arXiv:2008.12329
Cuadra, J., Armitage, P. J., Alexander, R. D., & Begelman, M. C. 2009, MNRAS, 393, 1423
Dermine, T., Izzard, R. G., Jorissen, A., & Van Winckel, H. 2013, A&A, 551, A50
Dey, L., Valtonen, M. J., Gopakumar, A., et al. 2018, ApJ, 866, 11
D'Orazio, D. J., Haiman, Z., & Schiminovich, D. 2015, Natur, 525, 351
Duffell, P. C., D'Orazio, D., Derdzinski, A., et al. 2020, ApJ, 901, 25
Farris, B. D., Duffell, P., MacFadyen, A. I., & Haiman, Z. 2014, ApJ, 783, 134
Farris, B. D., Duffell, P., MacFadyen, A. I., & Haiman, Z. 2015, MNRAS, 447, L80
Gayathri, V., Healy, J., Lange, J., et al. 2020, arXiv:2009.05461
Goldreich, P., & Tremaine, S. 1980, ApJ, 241, 425
Graham, M. J., Djorgovski, S. G., Stern, D., et al. 2015, MNRAS, 453, 1562
Haiman, Z., Kocsis, B., & Menou, K. 2009, ApJ, 700, 1952

Jensen, E. L. N., Dhital, S., Stassun, K. G., et al. 2007, AJ, 134, 241
Jorissen, A., Van Eck, S., Mayor, M., & Udry, S. 1998, A&A, 332, 877
Kelley, L. Z., Blecha, L., & Hernquist, L. 2017, MNRAS, 464, 3131
Kocsis, B., & Sesana, A. 2011, MNRAS, 411, 1467
Kóspál, Á, Ábrahám, P., Zsidi, G., et al. 2018, ApJ, 862, 44
Laine, S., Dey, L., Valtonen, M., et al. 2020, ApJL, 894, L1
Liao, W.-T., Chen, Y.-C., Liu, X., et al. 2020, MNRAS, submitted (arXiv:2008.12317)
Lubow, S. H., & Artymowicz, P. 1992, in Binaries as Tracers of Star Formation, ed. A. Duquennoy & M. Mayor (Cambridge: Cambridge Univ. Press), 145
Lubow, S. H., & Artymowicz, P. 1996, ASIC, 477, 53
MacFadyen, A. I., & Milosavljević, M. 2008, ApJ, 672, 83
Martín, E. L., Magazzù, A., Delfosse, X., & Mathieu, R. D. 2005, A&A, 429, 939
Mathieu, R. D., Adams, F. C., & Latham, D. W. 1991, AJ, 101, 2184
Mathieu, R. D., Stassun, K., Basri, G., et al. 1997, AJ, 113, 1841
Milosavljević, M., & Phinney, E. S. 2005, ApJL, 622, L93
Mingarelli, C. M. F. 2019, NatAs, 3, 8
Miranda, R., Muñoz, D. J., & Lai, D. 2017, MNRAS, 466, 1170
Muñoz, D. J., & Lai, D. 2016, ApJ, 827, 43
Muñoz, D. J., Lai, D., Kratter, K., & Mirand, A. R. 2020, ApJ, 889, 114
Muñoz, D. J., Miranda, R., & Lai, D. 2019, ApJ, 871, 84
Muzerolle, J., Flaherty, K., Balog, Z., Beck, T., & Gutermuth, R. 2019, ApJ, 877, 29
Oomen, G.-M., Pols, O., Van Winckel, H., & Nelemans, G. 2020, arXiv:2008.08097
Oomen, G.-M., Van Winckel, H., Pols, O., et al. 2018, A&A, 620, A85
Peters, P. C. 1964, PhRv, 136, 1224
Pols, O. R., Karakas, A. I., Lattanzio, J. C., & Tout, C. A. 2003, in ASP Conf. Ser. 303, Symbiotic Stars Probing Stellar Evolution, ed. R. L. M. Corradi, J. Mikolajewska, & T. J. Mahoney (San Francisco, CA: ASP), 290
Rafikov, R. R. 2016, ApJ, 830, 8
Robson, T., Cornish, N. J., & Liu, C. 2019, CQGra, 36, 105011
Roedig, C., Dotti, M., Sesana, A., Cuadra, J., & Colpi, M. 2011, MNRAS, 415, 3033
Romero-Shaw, I. M., Lasky, P. D., Thrane, E., & Calderon Bustillo, J. 2020, arXiv:2009.04771
Sesana, A. 2015, ASSP, 40, 147
Shi, J.-M., Krolik, J. H., Lubow, S. H., & Hawley, J. F. 2012, ApJ, 749, 118
Tang, Y., Haiman, Z., & MacFadyen, A. 2018, MNRAS, 476, 2249
Tang, Y., MacFadyen, A., & Haiman, Z. 2017, MNRAS, 469, 4258
Tiede, C., Zrake, J., MacFadyen, A., & Haiman, Z. 2020, ApJ, 900, 43
Tofflemire, B. M., Mathieu, R. D., Ardila, D. R., et al. 2017, ApJ, 835, 8
Waters, L. B. F. M., Cami, J., de Jong, T., et al. 1998, Natur, 391, 868